Ternary Mg-Nb-H polyhydrides under high pressure

Xilong Dou,[1,*] Xiaoyu Kuang,[1,*] Weiguo Sun ![ORCID],[2] Gang Jiang,[1] Cheng Lu,[2,†] and Andreas Hermann ![ORCID][3,‡]

[1]*Institute of Atomic and Molecular Physics, Sichuan University, Chengdu 610065, China*
[2]*School of Mathematics and Physics, China University of Geosciences (Wuhan), Wuhan 430074, China*
[3]*Centre for Science at Extreme Conditions and SUPA, School of Physics and Astronomy, The University of Edinburgh, Edinburgh EH9 3FD, United Kingdom*

Magnesium based alloys are promising solid materials for hydrogen storage. However, it is a real challenge to synthesise hydrogen storage materials with high hydrogen storage capacity and low dehydrogenation temperature. Here, we have performed extensively structural searches for ternary magnesium-based hydrogen storage compounds of Mg_7NbH_n with n ranging from 16 to 25 by CALYPSO method and first-principles calculations. We readily identified the experimentally observed Mg_7NbH_{16} hydride and uncovered a stable stoichiometry of Mg_7NbH_{19} with high hydrogen storage capacity of 6.7 wt% and low dehydrogenation temperature of 273 K. The remarkable decrease of the hydrogen release temperature is attributed to the atomic rearrangements in Mg_7NbH_{19}, which forms H-H pairs and has weakened metal-hydrogen chemical bonds compared to the stable Mg_7NbH_{16} and MgH_2 compounds. Our calculations show that Mg_7NbH_{16} undergoes a structural phase transition from its $P\bar{4}2m$ phase to a $Fm\bar{3}m$ phase at 75 GPa, and the $Fm\bar{3}m$ phase is a potential polyhydride superconductor. The present findings offer insights for understanding the hydrogen storage and release of Mg-Nb-H ternary magnesium-based hydrogen storage compounds, which open avenues for the design and synthesis of magnesium-based hydrogen storage material.

I. INTRODUCTION

Magnesium hydride MgH_2 is in principle a promising hydrogen storage material, made from abundant constituents and with a 7.7 wt% hydrogen storage capacity. However, the high thermodynamic stability and poor hydrogen sorption/desorption kinetics of MgH_2 require continued focus of attention and the search for simple and effective strategies to tune the material's properties. Although no final solutions have been found so far, continuous attempts over the past decade in materials chemistry and structure, such as alloying [1–5], catalyst additions [6], and targeted nano-structuring via various operations including ball-milling [7], solvent evaporation induced deposition [8], wet-chemical synthesis [9], mechanochemical methods [10], etc., have won considerable achievements. The hydrogen sorption/desorption kinetics performance of MgH_2 can be improved greatly by either reducing the grain size to the nanoscale or leading-in catalysts. Previous studies, however, suggest that the grain size needs to be regulated to 2 nm [11,12], which is difficult to achieve in term of current experimental equipment. Apart from technical difficulties, nanostructuring has little impact on thermodynamic properties [13]. Thus, focusing on introducing a suitable catalyst or dopant into MgH_2 could provide

more of an advantage in stimulating hydrogen kinetics and mitigating thermodynamic stability.

Niobium hydrides stand out in the field of hydrogen storage and attracted tremendous attention because of the extremely high mobility of hydrogen [14]. Situated in tetrahedral interstitial sites of niobium, hydrogen is very mobile at low temperature due to quantum tunneling [15,16]. In previous studies, Niobium and its oxides and fluoride have shown great potential to improve hydrogen transport kinetics if incorporated into the MgH_2 matrix. For instance, the milling time to create a Mg-Nb-H nanopowder, which exhibits excellent sorption kinetics, decreases significantly by using niobium oxide (Nb_2O_5) [17]. Full hydrogen desorption will be completed within 300 s at 300 °C by doping only 5 mol% Nb in MgH_2 [18]. So far, a number of technologies including *in situ* time-resolved x-ray scattering [19], x-ray diffraction (XRD) [20,21], x-ray photoelectron spectroscopy (XPS) [22], scanning and transmission electron microscopy (SEM and TEM) [20,23], x-ray absorption spectroscopy (XAS) [24], pressure-composition-temperature (PCT) [25], differential scanning calorimetry (DSC) [26], and Leco determinator [23] have been applied to track the dehydrogenation mechanism, hydrogen diffusion paths, desorption temperatures, and to investigate microstructure and hydrogen gravimetric density in the Mg-Nb-H system. These studies indicated that the destabilization of Mg-H bonding is due to multivalent Nb atom that facilitates charge transfer between Mg and H. Accelerated hydrogen release from MgH_2 is due to the formation of a metastable niobium hydride phase upon dehydrogenation, which establishes a gateway that facilitates hydrogen

---

*These authors contributed equally to this work.

†lucheng@calypso.cn

‡a.hermann@ed.ac.uk

emission. More recently, in a broader study of $Mg_xTM_{1-x}H_y$ (TM=Sc, Ti, V, Cr) systems, electrochemical measurements have indicated that for compositions $x \leqslant 0.8$, hydrogen transport kinetics was significantly enhanced [27]. Afterwards, by means of first principles calculation [28,29], reports related these improvements to structural transition from a rutile structure (favored by MgH_2) to a fluorite structure (favored by TMH_2). The latter is more suitable for reversible hydrogen storage and was therefore suggested as an essential factor in determining hydrogen storage properties. Accurate determination of the crystal structures of any hydride is a crucial first step to assess their usefulness as hydrogen storage material.

Among the Mg-Nb-H compounds, in particular, the analysis of temperature programmed desorption (TPD) found a surprising decrease in decomposition temperature by 140 K for Mg_7NbH_y, synthesized under ultrahigh pressure, in comparison with original MgH_2 [30]. Based on XRD measurements, experimental Mg_7NbH_{16} phases have been assigned a face-centered-cubic (fcc) structure with space group $Fm\bar{3}m$ with lattice parameters of $a = 9.563$ Å [30]. We are not aware of other experimental reports on the Mg_7NbH_{16} structure. Several computational studies have been carried out based on the assumption that the atomic occupancies of Mg_7NbH_{16} are identical to $Mg_{6.5}NbH_{14}$ [21,31,32], where Mg atoms occupy two inequivalent Wyckoff $4b$ and $24d$ sites, Nb atoms occupy $4a$ sites and all H atoms occupy tetrahedral holes ($32f$). Unexpectedly, our phonon calculations reveal that the above hypothesis is not true, as the appearance of imaginary frequencies suggests that the $Fm\bar{3}m$ phase is dynamically unstable at atmospheric pressure. In other words, the structural solution of Mg_7NbH_{16} remains an open question and requires further investigation. Aside from this, its thermodynamically preferred hydrogen release pathways are also poorly understood. From the viewpoint of practicability, optimization of its volumetric and gravimetric densities is a pressing need.

In the present paper, our goal is to find answers for the above requirements. Previously published theoretical works have shown that density-functional theory is perfectly capable of evaluating thermodynamic properties of various hydrogen storage materials and can assist in developing new hydrogen storage materials. Motivated by these facts, we perform a systematic investigation of ground-state structures and thermodynamic properties of Mg_7NbH_n ($n = 16–25$) using the Vienna *ab initio* simulation (VASP) package [33] in combination with the particle swarm optimization structure prediction (CALYPSO) code [34]. Our paper is organized as followed. In Sec. II, we discuss details of our calculations. In Sec. III, we describe the theoretically predicted compounds and discuss their structural features, thermal decomposition properties, electronic structures, bonding characteristics as well as superconducting properties for the magnesium niobium polyhydrogen system, making comparisons with available experimental data where possible. Finally all our findings are summarized and conclusions drawn in Sec. IV.

II. COMPUTATIONAL METHODS

We search for energetically favorable structures of Mg_7NbH_n (n = 16–25) with cell sizes up to 4 formula units

(f.u.) using the CALYPSO [34–36] code. The underlying calculations on structural relaxation, *ab initio* molecular dynamics (AIMD) simulations, electronic and elastic properties are performed with aid of the PBE exchange correlation functional [37–39], as implemented in the VASP package [33]. The valence space for Mg, Nb, H are $2p^63s^2$, $4s^24p^64d^45s^1$, and $1s^1$, respectively. Plane wave cutoff energy is set to 600 eV, and a Monkhorst-Pack Brillouin sampling grid with a resolution of 0.25 Å^{-1} is set to ensure the reliability of results. In AIMD simulations, a Nos$\acute{e}$ thermostat was used for controlling temperature in NVT ensemble. The initial temperature was set to 0 K, and then, in steps of 100 K, gradually increased to 500 K, with a relaxation times of 5 ps. For each intermediate temperature the system was equilibrated for 4 ps before the next temperature increase. We further employed the frozen phonon dynamical matrix approach to calculate the vibrational frequencies and subsequently used them to characterize finite-temperature vibrational enthalpies and vibrational entropies in the framework of the harmonic approximation. For H_2 gas, in addition to the static free energy obtained by placing a single molecule in a 10-Å cubic box, the contributions from translational ($3/2$ K_BT, where K_B represents the Boltzmann constant), rotational (K_BT), and pV degrees of freedom (K_BT) of H_2 are also taken into account. The entropy of the H_2 molecule is estimated using the expression for entropy of the ideal diatomic gas [40]. The phonon dispersion curves and electron-phonon coupling (EPC) calculations for the $Fm\bar{3}m$ phase at 75 GPa are calculated with the Quantum-ESPRESSO code [41]. Vanderbilt ultrasoft pseudopotentials within the framework of generalized gradient approximation correction of Perdew-Burke-Ernzerhof (GGA-PBE) [42,43], a kinetic energy cutoff of 50 Ry, 16 × 16 × 16 Monkhorst-Pack k-point sampling, and 4 × 4 × 4 q mesh were adopted in EPC calculations. The superconducting transition temperature (T_c) is estimated by means of the Allen-Dynes modified McMillan equation [44,45]

$$T_c = \frac{\omega_{log}}{1.2} \exp\left[-\frac{1.04(1+\lambda)}{\lambda - \mu^*(1+0.62\lambda)}\right], \quad (1)$$

where $\omega_{\log}$ is the logarithmic averaged frequency, μ^* is the Coulomb pseudopotential, and λ is the EPC constant. The $\omega_{\log}$ and λ can be calculated as [44,45]

$$\omega_{\log} = \exp[\frac{2}{\lambda}\int_0^\infty \frac{d\omega}{\omega}\alpha^2F(\omega)\ln(\omega)] \quad (2)$$

and

$$\lambda = 2\int_0^\infty \frac{\alpha^2F(\omega)}{\omega}d\omega \quad (3)$$

In Eqs. (2) and (3), $\alpha^2F(\omega)$ is Eliashberg EPC spectral function, which is defined as [44,45]

$$\alpha^2F(\omega) = \frac{1}{2\pi N_{E_F}}\sum_{qv}\frac{\gamma_{qv}}{\omega_{qv}}\delta(\omega - \omega_{qv}) \quad (4)$$

where N_{E_F} is the density of states at the Fermi Level, and the sum is over all phonon wave vectors q and branches v, while ω_{qv} is screened phonon frequency, and γ_{qv} is phonon

linewidth, which can be determined by [44,45]

$$\gamma_{qv} = 2\pi\omega_{qv}\sum_{mn\mathbf{k}}|g_{mn}^v(\mathbf{k},\mathbf{q})|^2\delta(\varepsilon_{m,\mathbf{k}+\mathbf{q}}-\varepsilon_F)$$
$$\times\,\delta(\varepsilon_{n,\mathbf{k}}-\varepsilon_F). \qquad (5)$$

The electron-phonon matrix elements $g_{mn}^v(\mathbf{k},\mathbf{q})$ is defined as [44,45]

$$g_{mn}^v(\mathbf{k},\mathbf{q}) = \left(\frac{\hbar}{2M\omega_{qv}}\right)^{\frac{1}{2}}\langle m,\mathbf{K}+\mathbf{q}|\delta_{qv}V_{\mathrm{SCF}}|n,\mathbf{k}\rangle. \qquad (6)$$

In Eq. (6), $\delta_{qv}V_{\mathrm{SCF}}$ is the derivative of the self-consistent potential with respect to the phonon displacement qv. The bare electronic Bloch state and ionic mass are labeled $|n,\mathbf{k}\rangle$ and M.

III. RESULTS AND DISCUSSION

A. Stability

We have performed structural searches at ambient pressure for Mg_7NbH_n compounds where n varies from 16 to 25 by using the CALYPSO method. For each composition, the resulting lowest-enthalpy structures are considered further, the structural parameters of which are listed in Table S1 within the Supplemental Material (SM) [46]. All considered structures are thermodynamically stable against breakdown into Mg, Nb, and H. On the basis of the known ground-state phases of related unary and binary compounds at ambient pressure, we constructed the ternary phase diagram to look for possible formation routes for these ternary hydrides, as depicted in Fig. 1(a). Obviously, the stoichiometry Mg_7NbH_{16} might be directly synthesized via $7*MgH_2+NbH_2$, while other stoichiometries are difficult to obtain in this way. Therefore, we calculated the enthalpy curves of relevant ternary $A+B+C \rightarrow D$ formation routes with respect to the predicted candidate structures as function of H content. As shown in Fig. 1(b), it can be seen that, apart from the stoichiometries of Mg_7NbH_{23} and Mg_7NbH_{24}, the mixing enthalpies suggest all candidate structures are thermodynamically stable against breakdown into pure Mg, pure Nb, or the hydrides NbH and NbH_2, and hydrogen, and could be obtained by directly mixing them. Figures 2(a), 2(b) and Fig. S1 within the SM [46] summarize calculated phonon dispersions for these considered structures. The absence of negative (imaginary) phonon frequencies for the Mg_7NbH_{16} and Mg_7NbH_{19} phase suggests that both compounds are dynamically stable at ambient pressure. On the basis of calculating the full elastic stiffness constants (see Table S2 within the SM [46]), we conclude that Mg_7NbH_{16} and Mg_7NbH_{19} phase are also mechanically stable [47]. The specific details of their respective mechanical stability criteria are described in the SM [46].

B. Mg_7NbH_{16}

As shown in Fig. 3(a), the ground-state structure of Mg_7NbH_{16} phase adopts space group $P\bar{4}2m$, containing 4 formula units per cell with lattice constants of $a = b = 9.451$ Å and $c = 9.461$ Å, all of which are quite close to the experimentally determined lattice constant of the $Fm\bar{3}m$ phase (9.563 Å) [30]. H atoms are evenly distributed around
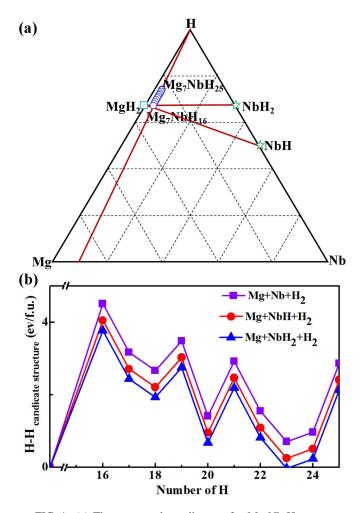

FIG. 1. (a) The ternary phase diagram for Mg-Nb-H system at ambient pressure. (b) Enthalpies per formula unit in Mg_7NbH_n (n = 16–25) as function of number of H with respect to the predicted candidate structures for each stoichiometry.

Mg and Nb atoms and occupy multiple $4n$ sites. Mg atoms at $8o$ sites are 7-fold coordinated with H atoms, forming an irregular heptahedron. Other Mg atoms are located at the $2f$, $1b$, $1d$, and $4n$ sites, respectively, and surrounded by four H atoms in tetrahedral coordination. The Nb atoms alternately fill the interstitial space between Mg atomic layers, sharing H atoms with the nearest neighboring Mg atoms and appear as either 8-fold or tetrahedrally coordinated. Note that in our searches we do not find the $Fm\bar{3}m$-Mg_7NbH_{16} phase reported in previous experimental and theoretical research at ambient pressure. This discrepancy might originate from finite temperature and pressure effects, which have not been taken into account in previous theoretical research and our work so far. In the light of above situation, we construct and calculate the $Fm\bar{3}m$ phase of Mg_7NbH_{16} as a comparison. The detailed structural information of this phase is given in Table S3 within the SM [46]. The optimized atom positions match well with earlier experimental and theoretical data [21,32]. The calculated formation energy implies that $Fm\bar{3}m$-Mg_7NbH_{16} is a metastable structure, which is 1.5 KJ/mol higher in energy than the $P\bar{4}2m$-Mg_7NbH_{16} structure. Subsequent calculations of the phonon dispersions demonstrate that the $Fm\bar{3}m$ phase
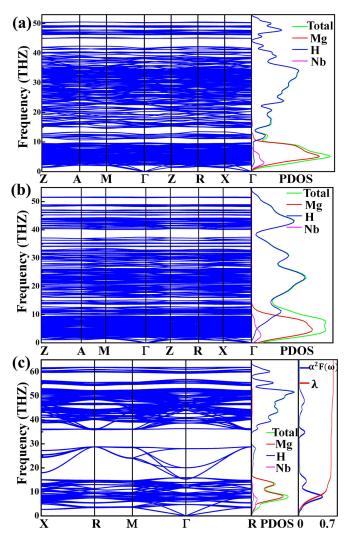
FIG. 2. (a) Phonon spectrum and projected phonon density of states (PHDOS) of (a) $P\bar{4}2m$-Mg$_7$NbH$_{16}$ at 0 GPa, (b) $P4_1$-Mg$_7$NbH$_{19}$ at 0 GPa, and (c) $Fm\bar{3}m$-Mg$_7$NbH$_{16}$ at 75 GPa.

FIG. 3. Crystal structures and local metal environments of Mg$_7$NbH$_{16}$ at (a) 0 GPa ($P\bar{4}2m$) and (b) 75 GPa ($Fm\bar{3}m$). Red, green, and yellow spheres represent Mg, Nb, and H atoms, respectively.

at 0 GPa is dynamically unstable (see Fig. S2 within the SM [46]). For this reason, the symmetry-reduced $P\bar{4}2m$ phase might provide a better explanation of the experimental observations. Unit cell parameters, in general, as determined experimentally by powder x-ray diffraction peaks can in many cases have nonunique solutions. To provide direct evidence for this hypothesis, we simulate the XRD spectra of $Fm\bar{3}m$-Mg$_7$NbH$_{16}$ and $P\bar{4}2m$-Mg$_7$NbH$_{16}$ in the 2θ range from 10° to 60°, and compare them to data from the experimental measurements in Fig. 4. As shown in Fig. 4, the seven diffraction peaks and relative intensities of the two phases line up extremely well, and in excellent agreement with the experimental pattern [30]. To some extent, this indicates that the structure observed in experiment might be the $P\bar{4}2m$ phase instead of $Fm\bar{3}m$. It should be stressed that temperature or pressure effects cannot be ruled out and might affect how calculations and experiments can be compared; for instance, many perovskite-like compounds feature high-temperature transitions to higher-symmetry structures. We therefore further explored the high-temperature evolution of the $P\bar{4}2m$
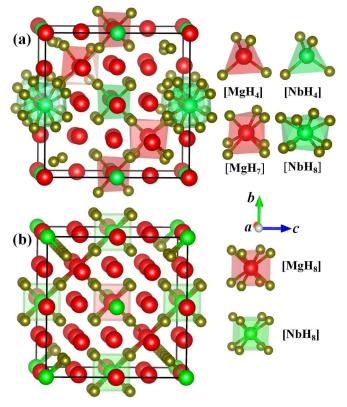
phase by AIMD calculations. The Mg-H and Nb-H partial distribution functions and coordination numbers (CN) in the temperature range from 0 K to 500 K are shown in Figs. S3(a) and S3(b) within the SM [46]. It is found that when the temperature increases to 100 K, the second and third Mg-H peaks turn into a broad shoulder following the first coordination peak, which in turn disappears at 300 K. As a consequence, the corresponding CN of Mg-H and Nb-H pairs evolve from 4-fold or 7-fold coordination to 8-fold coordination. These features are typical of the $P\bar{4}2m \rightarrow Fm\bar{3}m$ transition. Similar transitions to higher symmetry phases can also be induced by external compression. To probe the stability of the $P\bar{4}2m$ phase under pressure, we performed systematic structure
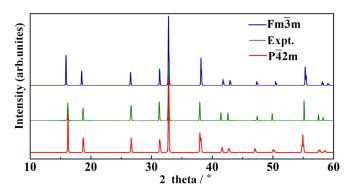

FIG. 4. Simulated XRD patterns for Mg$_7$NbH$_{16}$ with space group $P\bar{4}2m$ and $Fm\bar{3}m$ compared with experiment from Ref. [30].
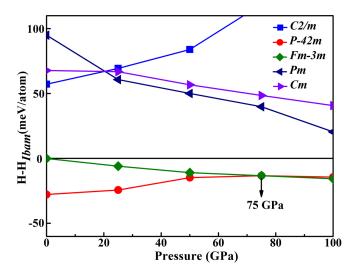
FIG. 5. Enthalpy curves per atom in Mg_7NbH_{16} as function of pressure relative to *Ibam* structure.

investigations for the stoichiometry of Mg_7NbH_{16} at select elevated pressures of 25, 50, 75, and 100 GPa. Figure 5 presents enthalpy curves per atom in Mg_7NbH_{16} as function of pressure for various candidate structures. The results suggest that the $P\bar{4}2m$ structure survives in the ground state up to 75 GPa, when it transforms into a cubic phase of $Fm\bar{3}m$ symmetry with lattice parameters of 8.045 Å. Subsequent calculations of elastic constants and phonon spectra indicate that $Fm\bar{3}m$ is stable at 75 GPa (see Fig. 2(c) and Table S2 within the SM [46]). Detailed information about the $Fm\bar{3}m$ phase at 75 GPa is displayed in Fig. 3(b) and Table S4 within the SM [46]. The Mg atoms occupy two different Wyckoff sites $4a$ and $24d$. Nb and H atoms occupy Wyckoff sites $4b$ and $32f$, respectively. Compared with the $P\bar{4}2m$ phase, pressure symmetrizes the 8-fold coordination of Mg and Nb atoms, with bond distances of 1.74 and 1.77 Å for the Mg-H and Nb-H bonds, respectively. All atomic positions in the $Fm\bar{3}m$ phase at 75 GPa are very close to the published experimental data. Such a result provides strong evidence that the $Fm\bar{3}m$ phase seen in experiment is due to pressure and finite temperature effects. It also demonstrates that the structure search scheme adopted by us is well suitable to survey the Mg-Nb-H system.

Having determined the crystal structure, we turn to discuss the thermodynamics of hydrogen desorption for the $P\bar{4}2m$ phase of Mg_7NbH_{16} at ambient pressure. Based on available experiment results [19,30], we have calculated vibrational zero point energies, vibrational enthalpies and vibrational entropies at T = 300 K for all known structures of reactants and products involved in the reactions. The obtained data are summarized in Table I. Here we do not take binary MgNb alloys into account, since experimental research has confirmed that it could not appear during the release of hydrogen [48]. In addition, experiments have reported the existence of $NbH_{0.6}$ in the process of decomposition of the magnesium niobium polyhydrogen system, while structure information for $NbH_{0.6}$ is not reported so far. Fortunately, qualitative analysis shows that it is similar to the Nb_4H_3 phase. Thus, in this paper we adopt the monoclinic phase of Nb_4H_3 phase in $P2$ symmetry to represent the $NbH_{0.6}$ phase, with details for its structural information as shown in Ref. [49]. From Table I we can see that the calculations on ZPE for several structures match very well with earlier DFT calculations [49–51] while our results for vibrational enthalpies and entropies at T = 300 K for Mg and MgH_2 phases are almost identical to results in Ref. [50]. In our calculations, Mg-Nb-H ternary phases have lower formation enthalpies relative to the MgH_2 phase, verifying that Nb can effectively reduce the thermodynamic stability of MgH_2. In Table II, we have listed the possible dehydrogenation pathways of Mg_7NbH_{16}, as well as the wt% H_2 release, reaction enthalpies and entropies and decomposition temperature at atmospheric pressure. The decomposition temperature is estimated on the basis of van't Hoff equation $\ln(p) = (-\Delta H/RT)+(\Delta S/R)$. For reference, we also investigate the dehydrogenation of MgH_2. As shown in Table II, our calculated results are in line with previous DFT calculations [50]. Note that the decomposition reaction $Mg_7NbH_{16} \rightarrow MgH_2+Nb+H_2$ has negative reaction enthalpy, i.e., is not thermodynamically favorable, thus this reaction is not included in Table II. Our results confirm the experimental observation that Nb precipitates until magnesium is completely dehydrogenated during hydrogen desorption from ternary Mg-Nb-H phases [19,30]. Moreover, considering the contribution of ZPE, we note that the reaction enthalpies decrease by 9 KJ/mol H_2, but taking the finite-temperature enthalpy contributions into account, the

TABLE I. The calculated formation energies at T=0K (in KJ/mol), ΔH, vibrational zero point energies (in KJ/mol), ZPE, vibrational enthalpies at T = 300 K (KJ/mol), $H_{vib}^{T=300K}$, and vibrational entropies (J/Kmol), $S_{vib}^{T=300K}$, for all compounds included in the decomposition reactions of the Mg-Nb-H system.

Compound	Space group	ΔH	ZPE	ZPE (other)	$H_{vib}^{T=300K}$	$S_{vib}^{T=300K}$
H_2		0.0	26.4	25.9 [51] 26.1 [50]	35.2	130.7
Mg	$P6_3/mmc$	0.0	2.9	2.9 [50]	7.9	31.3
Nb	$Im\bar{3}m$	0.0	2.6	2.4 [49]	7.8	34.7
MgH_2	$P4_2/mnm$	–62.9	38.0	39.1 [50]	44.4	31.0
Nb_4H_3	$P2$	–94.9	81.4		101.1	126.7
NbH_2	$Fm\bar{3}m$	–72.7	46.7	49.1 [49]	52.3	34.5
NbH	$Cccm$	–88.1	26.0	24.0 [49]	31.1	32.4
Mg_7NbH_{16}	$P\bar{4}2m$	–54.2	317.6		363.3	280.0
Mg_7NbH_{19}	$P4_1$	–35.3	362.3		416.2	333.5

TABLE II. Predicted decomposition reactions for ternary Mg-Nb-H phases. Listed are: the calculated wt% H_2 released, reaction enthalpies H at 0 K and 300 K (KJ/mol H_2), and reaction entropies S at 0 K and 300 K (J/K mol H_2), and reaction temperature T (K). Experimental results are given where available.

No.	Reaction	wt% H_2	$H_{T=0K}$	$H_{T=0K}^{ZPE}$	$H_{T=300K}$	$H_{T=300K}$ Expt.	$S_{T=300K}$	$S_{T=300K}$ Expt.	T
1	$MgH_2 \rightarrow Mg+H_2$	7.6	62.5	53.7	61.1	74.6 [50]	131.0	134.8 [50]	465
2	$4Mg_7NbH_{16} \rightarrow 28Mg+Nb_4H_3+61/2H_2$	5.5	52.3	42.7	50.3		126.8		397
3	$Mg_7NbH_{16} \rightarrow 7Mg+NbH_2+7H_2$	5.0	51.6	42.5	50.3		126.9		396
4	$Mg_7NbH_{16} \rightarrow 7Mg+NbH+15/2H_2$	5.6	52.6	42.6	50.9		126.7		401
4	$Mg_7NbH_{16} \rightarrow 7Mg+Nb+8H_2$	5.7	54.3	44.7	52.0		127.0		409
5	$4Mg_7NbH_{19} \rightarrow 28Mg+Nb_4H_3+73/2H_2$	6.5	32.9	22.4	31.3		121.6		257
6	$Mg_7NbH_{19} \rightarrow 7Mg+NbH_2+17/2H_2$	6.0	31.0	22.6	29.9		121.3		246
7	$Mg_7NbH_{19} \rightarrow 7Mg+NbH+9H_2$	6.4	32.5	223.8	31.1		121.6		256
8	$Mg_7NbH_{19} \rightarrow 7Mg+Nb+19/2H_2$	6.7	35.4	26.1	33.4		122.3		273

reaction enthalpies of these reactions are degenerate within 2 KJ/mol H_2. Through comparative analyses we find this enthalpy lowering effect might be caused exclusively by the ideal diatomic gas contribution to the enthalpies of free H_2 molecules, which is $7/2$ $K_B T$ in total. Another striking feature is that the decomposition temperature keeps constant in the decomposition of Mg_7NbH_{16} with respect to Nb_4H_3, NbH_2, or the NbH phases, with hydrogen loss 5.5 wt%, 5.0 wt%, and 5.6 wt%, respectively, as seen from reactions 2–4 in Table II. The thermodynamic hydrogen decomposition properties for $P\bar{4}2m$-Mg_7NbH_{16} are consistent with $MgNbH_2$, where the decomposition temperature remains constant when the metastable niobium phase appears in the process of H release [19]. This result suggests that no new compounds are synthesized during decomposition. The presence of a metastable niobium phase may be a collateral effect caused by the flow of hydrogen. Specifically, hydrogen atoms, stimulated by temperature, break from the bonds of Mg atoms and occupy a specific position in the niobium hydride phase, and then flow out of the matrix with the help of Nb. The steady flow of hydrogen atoms results in the present of a niobium phase. From reaction 3 in Table II we find that the presence of the NbH_2 structure occurs at 396 K. This decomposition temperature is different from the experimental observation (T = 523 K) [30], which might be partly due to the existence of kinetic barriers or impurities in the $MgNb_2H_n$ sample used in the experiments.

To provide further insights into the thermodynamic properties of the Mg_7NbH_{16} hydrides, we have calculated the electronic structure and projected density of states (PDOS) for both the $P\bar{4}2m$ structure under ambient pressure and $Fm\bar{3}m$ structure under 75 GPa, as shown in Figs. S4(a) and S4(b) within the SM [46]. The projections are onto spherical harmonics inside the different atoms' pseudopotential cutoff radii. The $P\bar{4}2m$ structure has semi-conducting character with a direct band gap at the Γ point (E_g=0.72 eV), while $Fm\bar{3}m$ is a metal with two bands crossing the Fermi level. From Figs. S4(a) and S4(b) within the SM [46], it is clear that the electronic states close to the Fermi level are derived from the Nb atoms. The valence states also show a dominant hydrogen feature, while conduction bands are dominated by Mg and Nb atoms. This is consistent with a picture of H^- anions and Mg/Nb cations. Compared with the original MgH_2

phase [52], the presence of Nb atoms in the $P\bar{4}2m$ phase of Mg_7NbH_{16} narrows the band gap. Calculations of the PDOS imply that Nb atoms inhibit hybridization between Mg and H atoms, transfer their electrons to H atoms instead of Mg, and further reduce the strength of the chemical bond between Mg and H atoms. The Mg-H bonds strength obtained from -COHP (crystal orbital Hamilton population [53]) calculations further verifies this point, which are illustrated in Fig. 6(a). In the Mg-Nb-H compounds, antibonding Mg-H contributions are at the Fermi level that are not present in MgH_2. Integrated -COHP values are in the range of 0.41–1 eV/bond in the
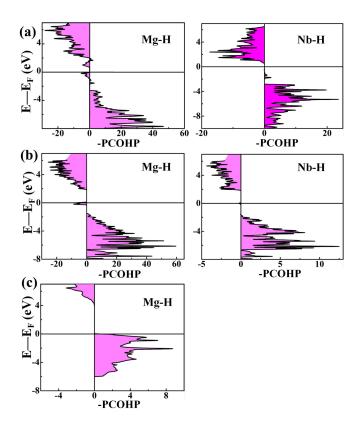

FIG. 6. Calculated -COHP curves for per Mg-H and Nb-H bond in unit cell: (a) -COHP for Mg_7NbH_{16}; (b) -COHP for Mg_7NbH_{19}, and (c) -COHP for MgH_2.

Mg_7NbH_{16} structure and 1.51–1.61 eV/bond in the MgH_2 structure, respectively. Nb-H interactions are far larger than Mg-H bonds, with corresponding average integrated COHP value of 2.4 eV/bond. To clearly illustrate the chemical bonding pattern, we employed the electronic localization function (ELF) and Bader charge to characterize the relative electron localization and charge transition for each crystal structure. As shown in Figs. S5(a) and S5(b) within the SM [46], the electrons near the sites of H atoms are highly localized, with the value of ELF close to 1.0 suggesting an electron pair on the anion sites, whereas at Mg sites the value of ELF is very low (0.2), consistent with empty valence shells. The ELF values (0.56) around Nb atoms demonstrate partial charge transfer from Nb to H. The Nb-H bonds strength in Mg_7NbH_{16} is almost identical to results in the NbH_2 structure [54]. From the Bader charge calculation, it is proposed that on average each Mg and Nb atom donates 1.62 e and 1.18 e to H atoms (see Table S5 within the SM [46]), respectively, in good agreement with the ELF results and suggesting that the bonding between metal ions and hydrogens is purely ionic. Comparing the ambient $P\bar{4}2m$ with 75 GPa $Fm\bar{3}m$ phase, it is proposed that the increasing pressure shortens the distance between Nb and H, restrains charge transfer and strengthens the interaction between Nb and H, leading to the transition from ionic bonding to partially metallic bonding.

Hydrogen-rich metal compounds are one of the best candidates for superconducting materials, which generally have high superconducting transition temperature. We therefore have carried out systematic EPC calculations for $Fm\bar{3}m$-Mg_7NbH_{16} at 75 GPa. Based on Eqs. (2) and (3), the EPC constant of λ and logarithmic averaged frequency ω_{log} are obtained to be 0.63 and 126.2, respectively. We then obtain the T_c of Mg_7NbH_{16} under 75 GPa by using Eq. (1) with $\mu^* = 0.12$. It is 2.7 K, which is close to T_c of NbH (1.5 K at 1 atm) and NbH_2 (< 2 K below 50 GPa) [49]. Like NbH and NbH_2 hydrides, the Fermi energy of Mg_7NbH_{16} is mainly associated with Nb 4d orbitals, with the value of 0.82 states/eV/cell, which contributes about 68% of total DOS at the Fermi energy. It is worth mentioning that the H-H distance in Mg_7NbH_{16} under 75 GPa is 2.04 Å, which is obviously longer than that of the Nb-H (1.77 Å) bond and result in a relatively small contributions to electron-phonon coupling from the hydrogen atoms. To explore the superconductivity mechanism of Mg_7NbH_{16} under high pressure, we further calculate the relations of Eliashberg spectral functions of $\alpha^2 F(\omega)$ and the cumulative EPC parameters of λ to finite frequencies by using Eqs. (3) and (4). The calculated results are shown in Fig. 2(c). Obviously, a large separation between high-frequency vibrations (>35 THz) and low-frequency vibrations (<28 THz) exists in the phonon dispersion curves of Mg_7NbH_{16} at 75 GPa. The EPC parameters λ increase with the increase of the phonon frequencies. Herein, the low-frequency vibrations, dominated by Mg and Nb atoms, provides the main contributions to the total EPC parameters of λ, which is 73%. By contrast, the high-frequency vibrations are mainly dominated by H atoms, which contributes only 27%. This is not surprising because an analysis of the PDOS of Mg_7NbH_{16} in Fig. S4(b) within the SM [46] indicates that, in contrast to LaH_{10} and H_3S [55,56], the contribution of H atoms to the DOS at the Fermi energy, about 20% of

TABLE III. Calculated DOS at the Fermi Level N_{E_F} (in states/eV/cell), electronphonon coupling constant λ, logarithmic-average phonon frequency ω_{log} (in K), and McMillan-Allen-Dynes superconducting T_c (in K).

Pressure	N_{E_F}				λ			ω_{log}	T_c
(GPa)	Mg	Nb	H	Total	Mg+Nb	H	Total		
75	0.15	0.82	0.24	4.15	0.46	0.17	0.63	126.2	2.7
150	0.09	0.55	0.55	1.89	0.25	0.26	0.51	840.5	6.2
250	0.10	0.40	0.54	1.34	0.29	0.20	0.49	873.2	7.0

the total DOS at the Fermi energy (Table III), is much less than that of the metal atoms (Mg and Nb) in Mg_7NbH_{16}, and the metallicity is dominated by the metal atoms. Essentially, the dominant contribution to superconducting pairing comes largely from the coupling of electronic and vibrational states of the metal atoms in Mg_7NbH_{16}, not from the H atoms, resulting in a low contribution to the electron-phonon coupling constant λ, and thus limiting the T_c owing to low Debye temperature caused by the heavy mass of Mg and Nb. It should be stressed that the phonons in the low-frequency region can not be separated into contributions assigned to Mg and Nb individually. As Papaconstantopoulos *et al.* [55] and Quan *et al.* [57] pointed out, this suggests that it is not possible to get the separate $\alpha^2 F(\omega)$ functions for Mg or Nb atoms, and thus separate their contributions to λ. Specifically, according to the Gaspari-Gyorffy (GG) theory [58–60], the Eq. (3) can be exact decoupled in terms of the density of states N_{E_F} at Fermi level, the atomic mass M, the second moment ω_2, and the average over the Fermi surface of the electron-ion matrix element $< I^2 >$, overall given by

$$\lambda = \frac{N_{E_F} < I^2 >}{M\omega_2^2}. \tag{7}$$

The scattering strength I^2 can be calculated as

$$I^2 = \langle\langle|\langle k|\frac{dV}{d\mathbf{R}}|k'\rangle|^2\rangle\rangle_{FS} \tag{8}$$

where V is crystal potential, $\mathbf{R}$ is the displacement of the atom, and the large brackets is a double average of $\mathbf{k}$, $\mathbf{k}'$ over the Fermi surface. A decoupling analysis of the EPC constant λ with respect to atom types is limited to a small number of compounds, with a characteristic separation of the phonon spectrum separating into distinct metal atom low-frequency and H high-frequency regimes, such as some X_nH_m binary compounds resembling H_3S or LaH_{10} [55,56,61]. In materials like Mg_7NbH_{16} where projected phonon DOS's from different atomic types overlap, it is not possible to achieve such a decomposition according to atomic types.

We now investigate the evolution of superconductivity of Mg_7NbH_{16} under high pressure. Our results show that the Mg_7NbH_{16} with $Fm\bar{3}m$ structure is stable under pressure up to 250 GPa (see Fig. S6 within the SM [46]). The detailed electron-phonon coupling (EPC) parameters of Mg_7NbH_{16} at 150 GPa and 250 GPa, including the project phonon density of states (PHDOS), Eliashberg spectral functions $\alpha^2 F(\omega)$ and EPC parameters $\lambda(\omega)$ are presented in Table III and

Fig. S7 within the SM [46]. It can be seen from Fig. S7 within the SM [46] that pressure promotes the high frequency vibrations, and the corresponding logarithmic averaged frequencies of $\omega_{\log}$ are increasing. In contrast, the total DOS at Fermi energy decrease monotonically as pressure increase. It is 4.15 states/eV/cell at 75 GPa, then decreases slightly to 1.89 states/eV/cell at 150 GPa, and then finally drops to 1.34 states/eV/cell at 250 GPa, which causes the decrease of λ with pressure increasing. Similar phenomena can be also observed in Ti(V)H$_3$ [62] and NbH$_2$ [49]. The T_c of Mg$_7$NbH$_{16}$ under high pressure is calculated to be 6.2 K at 150 GPa and 7.0 K at 250 GPa, respectively, which are comparable to those of vanadium hydrides [63], niobium hydrides [49] and titanium hydrides [62]. The DOS projections reveal that the contributions from hydrogenic states at the Fermi level is increased with pressure (see Table III and Fig. S8 within the SM [46]), which increases the contributions to the total λ from the H sublattice (51% at 150 GPa and 41% at 250 GPa), up from 27% at 75 GPa. The increased H-derived DOS at the Fermi level causes the relatively strong electron-phonon interactions and high T_c values of Mg$_7$NbH$_{16}$ at 150 GPa and 250 GPa compared to 75 GPa.

C. Mg$_7$NbH$_{19}$

The other energetically favorable compound, Mg$_7$NbH$_{19}$, adopts a tetragonal structure with $P4_1$ symmetry, shown in Fig. 7(a), in which all atoms occupy various crystallographic $4a$ sites. Each Nb atom is coordinated to eight H atoms and five Mg atoms, of which one participates in connecting NbH$_8$ units and itself forms an MgH$_6$ octahedron with six H atoms. A small number of H atoms are intercalated in voids in the structure in the form of H$_2$ molecules. Their respective H-H distance is 0.75 Å, and they are highlighted with the blue circle in Fig. 7(a). Remaining Mg atoms form irregular coordination polyhedra with five H atoms. Similar to the stoichiometry Mg$_7$NbH$_{16}$, we search for stable high-pressure structures of Mg$_7$NbH$_{19}$ at fixed pressure of 25, 50, 75, and 100 GPa. The relative formation enthalpies of predicted structures as function of pressure, against a particular candidate of $P\text{-}4$ symmetry, are plotted in Fig. 7(b). The $P4_1$ structure remains the lowest-enthalpy structure up to at least 100 GPa. Table I presents the calculation results for Mg$_7$NbH$_{19}$ on formation enthalpy, ZPE, vibrational enthalpies and vibrational entropies at T = 300 K. A notable feature is the big enthalpic difference ($\sim$19 KJ/mol H$_2$) between Mg$_7$NbH$_{16}$ and Mg$_7$NbH$_{19}$. From the crystal structures in Figs. 3(a) and 7(a), we deduce this behavior may be mainly due to the number of hydrogen molecules in the matrix of the latter. From Table I, we predict the thermodynamic properties for the $P4_1$ phase of Mg$_7$NbH$_{19}$ during hydrogen desorption at ambient pressure. Shown as reactions 6–9 in Table II, just like the stoichiometries of Mg$_7$NbH$_{16}$ and MgNbH$_2$, predicted decomposition temperatures remain constant. A Nb phase precipitates until magnesium is completely dehydrogenated. Any metastable niobium phase is the product of the flow of hydrogen. Our results verify there exists a dehydrogenation gateway through formation of metastable niobium-hydride phases in the magnesium niobium polyhydrogen system. It is particularly noteworthy that we find a desirable reaction enthalpy of
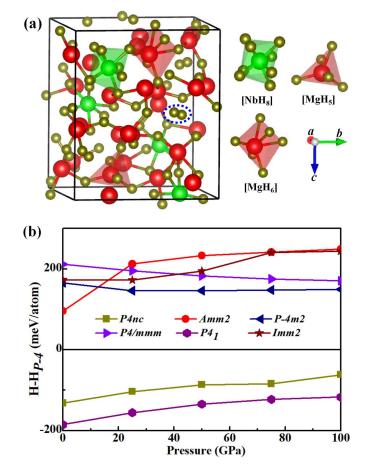

FIG. 7. (a) Crystal structure and local metal environments of Mg$_7$NbH$_{19}$ at ambient pressure. (b) Relative formation enthalpies per atom in Mg$_7$NbH$_{19}$ as function of pressure.

33 KJ/mol H$_2$ in the decomposition of the Mg$_7$NbH$_{19}$ phase, which is very close to the ideal range of reaction enthalpy (20–30 KJ/mol H$_2$) [64], see reactions 6–8 in Table II. From a thermodynamic perspective, reaction 9 in Table II indicates that it is able to precipitate metal Mg and Nb phase, along with 6.7 wt% hydrogen release. Note that all decompositions have lower reaction enthalpies in comparison with the standard entropy of H$_2$ gas, as previously suggested by other theoretical groups [65,66]. One straight forward explanation could be that this is due to the different numbers of low frequency rotational and translational terms between reactants and products. The increased contribution of hydrogen atoms to low frequency vibrations further reduces the entropy for the Mg$_7$NbH$_{19}$ phase [Figs. 2(a) and 2(b)], and shifts ΔS by 5 J/Kmol relative to Mg$_7$NbH$_{16}$ phase as shown in Table II. Our results suggest that improvement of hydrogen storage performance can be achieved by varying the content of hydrogen in system. This may be a valid argument, because adjustment of molar ratio in compounds directly affects the distribution of vibration frequencies and leads to the changes in formation enthalpies and entropies, in particular for the H atoms. In fact, there is a precedent for this kind of behavior, where different authors have found different dehydrogenation mechanisms, dehydrogenation temperatures and dehydrogenation contents using different molar stoichiometric ratios [67,68].

Figure S4(c) within the SM [46] presents the band structure and density of states for the $P4_1$-Mg_7NbH_{19} phase. Similar to the $P\bar{4}2m$-Mg_7NbH_{16} compound, the $P4_1$ phase exhibits semiconducting character, with an indirect band gap of 1.75 eV. The occupied states mainly originate from Nb and H. The PDOS of the $P4_1$ phase suggests that hybridization between Nb and H occurs in the –2 to –8 eV range. The results for -COHP calculations on nearest neighbor Mg-H and Nb-H pairs in the Mg_7NbH_{19} phase are plotted in Fig. 6(b). The corresponding integrated -COHP values are distributed across the ranges of 0.33–1.23 and 2.32–2.52 eV/bond, which is almost equal to the Mg-H and Nb-H interactions in the Mg_7NbH_{16} phase. In the Mg_7NbH_{19} phase, an obvious feature is that Mg-H and Nb-H anti-bonding states occupy the highest valence band. Such a result is known to decrease the electronic energy and therefore the stability of the electronic system [69,70], which correlates with the enthalpy difference between $P4_1$ and $P\bar{4}2m$ phase. The ELF results (see Fig. S5 within the SM [46]) show that its values at the atomic H sites is close to 1 and electrons are well localized, consistent with H^- anions. Meanwhile the ELF at either Mg sites or interstitial areas between Mg and H is almost close to 0, which reveals that the Mg-H bonds are ionic. Compared to $P\bar{4}2m$-Mg_7NbH_{16}, Bader charges suggest less charge transfer from Mg to H, with average charge of $+1.58\ e$ per Mg atom. The hydrogen molecules embedded in structural voids are bound by covalent bonds, corresponding to ELF values of 0.99, in good agreement with the Bader charge conclusion (see Table S5 within the SM [46]). However, the changes to Nb-H bonds are different, as the ELF value (0.66) at mid-point of Nb-H bonds in the $P4_1$ phase is slightly higher than in the $P\bar{4}2m$ phase, and transferring 1.06 e to H atoms. From Bader and ELF results, we can conclude that, with respect to $P\bar{4}2m$-Mg_7NbH_{16}, one might reason for the reduction of the charge transfer values in $P4_1$-Mg_7NbH_{19} is the hydrogen molecules. These hydrogen molecules are basically neutral, and achieve self-balancing by sharing electrons within themselves, reducing the charge demand to balance the overall crystal. In addition, comparing $P\bar{4}2m$-Mg_7NbH_{16} with the $P4_1$-Mg_7NbH_{19} compound, the additional injection of H into the Mg-Nb-H system helps to strengthen Nb-H bonds. This is not in contradiction to our conclusions presented earlier: Nb acts as gateway for hydrogen motion in the magnesium niobium polyhydrides system, thus finite strengthening of Nb-H bonds is ultimately more favorable for hydrogen desorption.

IV. CONCLUSION

In summary, we have reported a comprehensive theoretical study of ternary Mg-Nb-H polyhydrides and uncover a stable stoichiometry of Mg_7NbH_{19} with $P4_1$ symmetry under ambient pressure by CALYPSO method and first-principles calculations. The calculated results indicate that the Mg_7NbH_{19} compound is an ideal magnesium-based hydrogen storage alloy that exhibits excellent hydrogen storage properties with high hydrogen storage capacity of 6.7 wt% and remarkably low hydrogen release temperature of 273 K, which is due to the existence of H_2 molecules that reduce the interactions between metal and hydrogen atoms. Furthermore, the phonon dispersion curves, formation energy and XRD as well as AIMD results indicate that the ground-state structure of Mg_7NbH_{16} at 0 K is $P\bar{4}2m$ symmetry under ambient pressure, which is highly sensitive to temperature and translate to $Fm\bar{3}m$ at the temperature above 300 K. In addition, we concluded the $P\bar{4}2m$ phase transforms to the $Fm\bar{3}m$ phase above 75 GPa accompanied by a semiconductor-metal transition. The $Fm\bar{3}m$ phase of Mg_7NbH_{16} is a potential polyhydride superconductor with T_c about 2.7 K at 75 GPa. These results elucidate the structural and hydrogen storage properties of Mg-Nb-H ternary magnesium-based hydrogen storage compounds, and offer crucial insights to help guide future developments toward practical hydrogen storage materials.

[1] N. L. Rosi, J. Eckert, M. Eddaoudi, D. T. Vodak, J. Kim, M. O'keeffe, and O. M. Yaghi, Science **300**, 1127 (2003).

[2] P. Chen, Z. Xiong, J. Luo, J. Lin, and K. L. Tan, Nature (London) **420**, 302 (2002).

[3] Z. Shao, D. Duan, L. Wang, H. Song, H. Yu, Y. Yao, and T. Cui, Phys. Rev. B **104**, 054110 (2021).

[4] A. J. Samin, D. A. Andersson, E. F. Holby, and B. P. Uberuaga, Phys. Rev. B **99**, 014110 (2019).

[5] Y. Zhang, F. Majzoub, V. Ozoliņš, and C. Wolverton, Phys. Rev. B **82**, 174107 (2010).

[6] X. Huang, X. Xiao, X. Wang, Z. Yao, C. Wang, X. Fan, and L. Chen, Energy Stor. Mater. **13**, 199 (2018).

[7] Z. Ding, Y. Lu, L. Li, and L. Shaw, Energy Stor. Mater. **20**, 24 (2019).

[8] Y. Huang, G. Xia, J. Zhang, Z. Guo, and X. Yu, Energy Stor. Mater. **17**, 178 (2019).

[9] K. Jeon, H. R. Moon, A. M. Ruminski, B. Jiang, C. Kisielowski, R. Bardhan, and J. J. Urban, Nat. Mater. **10**, 286 (2011).

[10] M. Paskevicius, D. A. Sheppard, and C. E. Buckley, J. Am. Chem. Soc. **132**, 5077 (2010).

[11] R. W. Wagemans, J. H. Lenthe, P. E. de Jongh, A. J. Van Dillen, and K. P. De Jong, J. Am. Chem. Soc. **127**, 16675 (2005).

[12] Z. G. Wu, M. D. Allendorf, and J. C. Grossman, J. Am. Chem. Soc. **131**, 13918 (2009).

[13] N. S. Norberg, T. S. Arthur, S. J. Fredrick, and A. L. Prieto, J. Am. Chem. Soc. **133**, 10679 (2011).

[14] J. Engelhard, J. Phys. F **9**, 2217 (1979).

[15] H. Wipf and K. Neumaier, Phys. Rev. Lett. **52**, 1308 (1984).

[16] A. Weidinger and R. Peichl, Phys. Rev. Lett. **54**, 1683 (1985).

[17] J. Huot, J. F. Pelletier, L. B. Lurio, M. Sutton, and R. Schulz, J. Alloy Compd. **348**, 319 (2003).

[18] O. Friedrichs, J. C. Sanchezlopez, C. Lopezcartes, T. Klassen, R. Bormann, and A. Femandez, J. Phys. Chem. B **110**, 7845 (2006).

[19] J. F. Pelletier, J. Huot, M. Sutton, R. Schulz, A. R. Sandy, L. B. Lurio, and S. G. Mochire, Phys. Rev. B **63**, 052103 (2001).

[20] N. Bazzanella, R. Checchetto, and A. Miotello, Appl. Phys. Lett. **85**, 5212 (2004).

[21] T. Sato, D. Kyoi, E. Ronnebro, N. Kitamura, T. Sakai, and D. Noreus, J. Alloys Compd. **417**, 230 (2006).

[22] L. Zhang, X. Xiao, C. Xu, J. Zheng, X. Fan, J. Shao, S. Li, H. Ge, Q. Wang, and L. Chen, J. Phys. Chem. C **119**, 8554 (2015).

[23] J. F. De Castro, S. F. Santos, A. L. Costa, A. R. Yavari, and T. T. Ishikawa, J. Alloys Compd. **376**, 251 (2004).

[24] N. Hanada, T. Ichikawa, S. Isobe, T. Nakagawa, K. Tokoyoda, T. Honma, H. Fujii, and Y. Kojima, J. Phys. Chem. C **113**, 13450 (2009).

[25] C. Cheng, M. Chen, X. Xiao, X. Huang, J. Zheng, and L. Chen, J. Phys. Chem. C **122**, 7613 (2018).

[26] Y. Luo, P. Wang, L. Ma, and H. Cheng, J. Alloys Compd. **453**, 138 (2008).

[27] R. A. H. Niessen and P. H. L. Notten, Solid State Lett. **8**, A534 (2005).

[28] S. Er, D. Tiwari, G. A. de Wijs, and G. Brocks, Phys. Rev. B **79**, 024105 (2009).

[29] S. X. Tao, P. H. L. Notten, R. A. van Santen, and A. P. J. Jansen, Phys. Rev. B **82**, 125448 (2010).

[30] D. Kyoi, N. Kitamura, H. Tanaka, A. Ueda, S. Tanase, and T. Sakai, J. Alloys Compd. **428**, 268 (2007).

[31] M. G. Shelyapina, D. Fruchart, and P. Wolfers, Int. J. Hydrogen Energy **35**, 2025 (2010).

[32] Y. Bouhadda, M. Bououdina, N. Fenineche, and Y. Boudouma, J. Renewable Energies **18**, 503 (2015).

[33] G. Kresse and J. Furthmüller, Phys. Rev. B **54**, 11169 (1996).

[34] Y. Wang, J. Lv, L. Zhu, and Y. Ma, Comput. Phys. Commun. **183**, 2063 (2012).

[35] W. Sun, X. Kuang, H. D. J. Keen, C. Lu, and A. Hermann, Phys. Rev. B **102**, 144524 (2020).

[36] B. Chen, L. J. Conway, W. Sun, X. Kuang, C. Lu, and A. Hermann, Phys. Rev. B **103**, 035131 (2021).

[37] J. P. Perdew, J. A. Chevary, S. H. Vosko, K. A. Jackson, M. R. Pederson, D. J. Singh, and C. Fiolhais, Phys. Rev. B **46**, 6671 (1992).

[38] C. Lu, W. Gong, Q. Li, and C. Chen, J. Phys. Chem. Lett. **11**, 9165 (2020).

[39] C. Lu and C. Chen, J. Phys. Chem. Lett. **12**, 2848 (2021).

[40] K. J. Michel, A. R. Akbarzadeh, and V. Ozolins, J. Phys. Chem. C **113**, 14551 (2009).

[41] P. Giannozzi, S. Baroni, N. Bonini, M. Calandra, R. Car, C. Cavazzoni, D. Ceresoli, G. L. Chiarotti, M. Cococcioni, and I. Dabo, J. Phys. Condens. Matter. **21**, 395502 (2009).

[42] J. P. Perdew, K. Burke, and M. Ernzerhof, Phys. Rev. Lett. **77**, 3865 (1996).

[43] D. Vanderbilt, Phys. Rev. B **41**, 7892 (1990).

[44] P. B. Allen and R. C. Dynes, Phys. Rev. B **12**, 905 (1975).

[45] P. B. Allen, Phys. Rev. B **6**, 2577 (1972).

[46] See Supplemental Material at http://link.aps.org/supplemental/10.1103/PhysRevB.104.224510 for structural and electronic properties of Mg-Nb-H polyhydrides.

[47] Z. J. Wu, E. J. Zhao, H. P. Xiang, X. F. Hao, X. J. Liu, and J. Meng, Phys. Rev. B **76**, 054115 (2007).

[48] E. Rönnebro, D. Kyoi, A. Kitano, Y. Kitano, and T. Sakai, J. Alloys Compd. **404**, 68 (2005).

[49] G. Gao, R. Hoffmann, N. W. Ashcroft, H. Liu, A. Bergara, and Y. Ma, Phys. Rev. B **88**, 184104 (2013).

[50] A. R. Akbarzadeh, V. Ozolins, and C. M. Wolverton, Adv. Mater. **19**, 3233 (2007).

[51] K. Miwa, N. Ohba, S. Towata, Y. Nakamori, and S. Orimo, Phys. Rev. B **69**, 245120 (2004).

[52] P. Vajeeston, P. Ravindran, A. Kjekshus, and H. Fjellvag, Phys. Rev. Lett. **89**, 175506 (2002).

[53] R. Dronskowski and P. E. Blochl, J. Phys. Chem. **97**, 8617 (1993).

[54] C. Zhang, G. Sun, J. Wang, C. Lu, Y. Jin, X. Kuang, and A. Hermann, ACS Appl. Mater. Inter. **9**, 26169 (2017).

[55] D. A. Papaconstantopoulos, B. M. Klein, M. J. Mehl, and W. E. Pickett, Phys. Rev. B **91**, 184511 (2015).

[56] D. A. Papaconstantopoulos, M. J. Mehl, and P. H. Chang, Phys. Rev. B **101**, 060506(R) (2020).

[57] Y. Quan, S. S. Ghosh, and W. E. Pickett, Phys. Rev. B **100**, 184505 (2019).

[58] W. L. McMillan, Phys. Rev. **167**, 331 (1968).

[59] J. J. Hopfield, Phys. Rev. **186**, 443 (1969).

[60] G. D. Gaspari and B. L. Gyorffy, Phys. Rev. Lett. **28**, 801 (1972).

[61] A. M. Shipley, M. J. Hutcheon, R. J. Needs, and C. J. Pickard, Phys. Rev. B **104**, 054501 (2021).

[62] Q. Zhuang, X. Jin, T. Cui, D. Zhang, Y. Li, X. Li, K. Bao, and B. Liu, Phys. Rev. B **98**, 024514 (2018).

[63] X. Li and F. Peng, Inorg. Chem. **56**, 13759 (2017)

[64] J. Yang, A. Sudik, C. Wolverton, and D. Siegl, J. Chem. Soc. Rev. **39**, 656 (2010).

[65] V. Ozoliņš, E. H. Majzoub, and C. Wolverton, J. Am. Chem. Soc. **131**, 230 (2009).

[66] A. R. Akbarzadeh, C. M. Wolverton, and V. Ozolins, Phys. Rev. B **79**, 184102 (2009).

[67] Y. Nakamori, G. Kitahara, K. Miwa, N. Ohba, T. Noritake, S. Towata, and S. Orimo, J. Alloys Compd. **404**, 396 (2005).

[68] B. Zhang and Y. Wu, Int. J. Hydrog. Energy **39**, 13603 (2014).

[69] A. Decker, G. A. Landrum, and R. Dronskowski, Z. Anorg. Allg. Chem. **628**, 295 (2002).

[70] A. K. Verma and P. A. Modak, Phys. Chem. Chem. Phys. **20**, 26344 (2018).